Front. Phys. 13(3), 137805 (2018)
https://doi.org/10.1007/s11467-018-0790-2

First-principles calculations of nitrogen-doped antimony triselenide: A prospective material for solar cells and infrared optoelectronic devices

Sajid-ur-Rehman[1,2,8], **Faheem K. Butt**[3,4,†], **Chuanbo Li**[1,5,‡],
Bakhtiar Ul Haq[6,7], **Zeeshan Tariq**[1,2], **F. Aleem**[8]

[1] *State Key Laboratory on Integrated Optoelectronics, Institute of Semiconductors, Chinese Academy of Sciences; College of Materials Science and Opto-Electronic Technology, University of Chinese Academy of Sciences, Beijing* 100083, *China*
[2] *University of Chinese Academy of Sciences, Beijing* 100049, *China*
[3] *Department of Physics, Division of Science and Technology, University of Education,*
College Road, Township, Lahore 54770, *Pakistan*
[4] *Physik-Department, ECS, Technische Universität München, James-Franck-Str. 1, D-85748 Garching, Germany*
[5] *School of Science, Minzu University of China, Beijing* 100081, *China*
[6] *Advanced Functional Materials & Optoelectronics Laboratory (AFMOL), Department of Physics, Faculty of Science,*
King Khalid University, P.O. Box 9004, Abha, Saudi Arabia
[7] *Research Center for Advanced Materials Science (RCAMS), King Khalid University,*
Abha 61413, P.O. Box 9004, Saudi Arabia
[8] *Department of Physics, The University of Lahore, 1-Km Raiwind Road, Lahore* 53700, *Pakistan*
Corresponding authors. E-mail: †*faheemk.butt@ue.edu.pk,* ‡*cbli@semi.ac.cn*

Received April 17, 2017; accepted October 5, 2017

This study is focused on calculation of the electronic structure and optical properties of non-metal doped $\mathrm{Sb_2Se_3}$ using the first-principles method. One and two N atoms are introduced to Sb and Se sites in a $\mathrm{Sb_2Se_3}$ crystal. When one and two N atoms are introduced into the $\mathrm{Sb_2Se_3}$ lattice at Sb sites, the electronic structure shows that the doping significantly modifies the bandgap of $\mathrm{Sb_2Se_3}$ from 1.11 eV to 0.787 and 0.685 eV, respectively. When N atoms are introduced to Se sites, the material shows a metallic behavior. The static dielectric constants $\epsilon_1(0)$ for $\mathrm{Sb_{16}Se_{24}}$, $\mathrm{Sb_{15}N_1Se_{24}}$, $\mathrm{Sb_{14}N_2Se_{24}}$, $\mathrm{Sb_{16}Se_{23}N_1}$, and $\mathrm{Sb_{16}Se_{22}N_2}$ are 14.84, 15.54, 15.02, 18.9, and 39.29, respectively. The calculated values of the refractive index $n(0)$ for $\mathrm{Sb_{16}Se_{24}}$, $\mathrm{Sb_{15}N_1Se_{24}}$, $\mathrm{Sb_{14}N_2Se_{24}}$, $\mathrm{Sb_{16}Se_{23}N_1}$, and $\mathrm{Sb_{16}Se_{22}N_2}$ are 3.83, 3.92, 3.86, 4.33, and 6.21, respectively. The optical absorbance and optical conductivity curves of the crystal for N-doping at Sb sites show a significant redshift towards the short-wave infrared spectral region as compared to N-doping at Se sites. The modulation of the static refractive index and static dielectric constant is mainly dependent on the doping level. The optical properties and bandgap narrowing effect suggest that the N-doped $\mathrm{Sb_2Se_3}$is a promising new semiconductor and can be a replacement for GaSb due to its very similar bandgap and low cost.

Keywords $\mathrm{Sb_2Se_3}$, infrared, optical properties, solar cells, optoelectronic devices

PACS numbers 78.20.-e, 84.60.jt, 85.60.-q

1 Introduction

Despite the increase in the solar energy consumption, about 2.0×10^{19} J of energy is still wasted every hour out of 4.1×10^{20} J consumed on Earth every year [1]. Hence, there is a big difference between our current use of solar energy and its potential applications, which manifests the major challenge in energy research. Antimony selenide is an orthorhombic layered structure semiconductor and belongs to the $\mathrm{V_2}$-$\mathrm{Vl_3}$ family [2–5], which is known to include intriguing materials with excellent photovoltaic, thermoelectric, and electrochemical properties [6–8]. $\mathrm{Sb_2Se_3}$ has attracted attention due its amorphous and crystalline material properties with an associated switching effect [9], which has potential applications in thermoelectric cooling and optical devices [10, 11], memory switching devices [12], optical coatings [13], and photovoltaic conversion devices [14, 15]. The theoretically predicted efficiency of nanostructured Sb_2Se_3 solar cells is greater than 20% [16, 17]. Furthermore, Sb and Se have low toxicity and are abundant materials, making Sb_2Se_3 very promising for photovoltaics and other optoelectronic applications.

A review of the literature shows that single-crystal Sb_2Se_3 has a bandgap from ~ 1 to 1.82 eV [18]. The earlier study related to the nature of the bandgap indicates that Sb_2Se_3 is a direct bandgap [19] material, but in literature (experimental and theoretical) it is also reported as an indirect bandgap material [4, 20]. Although there is a controversy about the nature of the bandgap due to the extremely small difference between indirect and direct bandgaps [18], Sb_2Se_3 is reported in literature mostly as an indirect bandgap material [3, 4, 18, 20–22], including our results. In order to utilize the maximum spectral range in the solar spectrum, the bandgap of Sb_2Se_3 should be tuned, which will broaden the operational optical window of the Sb_2Se_3-based optoelectronic devices.

Nowadays, doping is one of the well-developed processes to improve the surface structure and properties of materials. Doping can dramatically modify physical and chemical properties of materials [23]. Therefore, Sb_2Se_3 is repeatedly doped with different metals and transition elements to tune its bandgap and enhance its optical, electrical, and magnetic properties [24–27]. Nonmetal doping is another approach used to narrow the bandgap; in comparison to metal doping that often forms a donor level in the forbidden band, non-metal doping usually shifts the valence band edge upward [28]. Doping with non-metal elements such as N shows an enhancement in the electronic, optical, and magnetic properties of narrow-bandgap semiconductor materials [29–32]. The doping by N has also shown higher thermal stability and conductivity in graphene [33]. The aforesaid reasons motivated us to study the doping by nitrogen atoms, which can significantly modify/tune the electronic and optical properties of Sb_2Se_3. To the best of our knowledge, no studies on N-doped Sb_2Se_3 exist in literature. Those currently under-the-investigated photoactive materials and their inside micro- or nano-scale structures are also required to be optimized, in order to ensure a lower enough recombination rate of the photon-generated electrons and holes [34]. The nitrogen doping approach in Sb_2Se_3 may open new paths to non-metal elements doping for various other potential applications such infrared detectors, infrared LEDs, lasers, transistors, and thermo-photovoltaic systems.

In the present work, first-principles calculations are performed on N-doped Sb_2Se_3. Through the band structure and optical properties (dielectric function, refractive index, absorption spectrum, and optical conductivity) calculations for different doping levels in N-doped Sb_2Se_3, useful theoretical information is obtained. These studies provide a fundamental basis for non-metal doping in chalcogenides systems for exploitation in corresponding infrared/mid-infrared optoelectronic devices.

2 Computational method

First-principles calculations using a supercell approach are performed to study the electronic structure as well as optical properties of the non-metal doped Sb_2Se_3. During the calculations, for the construction of pure Sb_2Se_3, a super-cell with 40 atoms and dimensions of $1\times1\times2$ was used. To build the doped models, one and two Sb and Se atoms are substituted by one and two N atoms. Three models of $Sb_{16}Se_{24}$, $Sb_{15}N_1Se_{24}$, and $Sb_{16}Se_{23}N_1$ are displayed in Figs. 1(a)–(c), respectively, and two other models of $Sb_{15}N_2Se_{24}$ and $Sb_{16}Se_{23}N_2$ are described in the supplementary information (Fig. S1). In the calculations, we used the crystallographic information file (CIF) for Sb_2Se_3 as introduced previously [35]. The CIF is generated from the experimental information [36].

The first-principles calculations are carried out using CASTEP [37] code working within Material Studio environment based on an approach called plane-wave pseudopotential in the context of density functional theory (DFT). The pseudopotential method is efficient and fast due to the fact that no prior shape approximation of the orbitals is required. Sb and Se have $5s2$ $5p3$ and $4s2$ $4p4$ electronic configurations, respectively. Exchange-correlation energy was treated in the Wu-Cohen's generalized gradient approximation (WC-GGA) [38] for the lattice dynamics of Sb_2Se_3 [18, 39–43]. A 320 eV cutoff energy and a Monkhorst pack grid of $1 \times 1 \times 2$ k points were used to integrate the Brillouin zone. The self-consistent convergence accuracy was set at 1×10^{-6} eV/atom. The convergence criterion for the key force on atoms was 0.05 eV/Å, the value of stress was 0.1 GPa, and the maximum displacement was 2×10^{-4} nm. The optical properties (dielectric constants, refractive index, absorption coefficient, and optical conductivity) were calculated with a fine mesh of $2\times2\times3$ for the summation over the Brillion zone. The structures of undoped and doped $Sb_{16}Se_{24}$ supercells were optimized in order to determine the influence of impurities on the stability of the structure. The supercell structures were optimized first, and the lattice parameters were obtained. The radius of N (0.74 Å) is smaller than that of Sb (1.41 Å) when N is occupying the Sb and Se sites, which leads to the decreasing cell vectors. For more accurate results, we

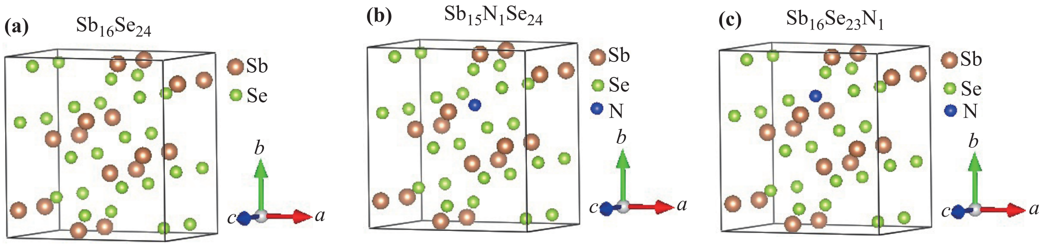

Fig. 1 $Sb_{16}Se_{24}$ supercell models: **(a)** Undoped $Sb_{16}Se_{24}$ supercell, **(b)** $Sb_{15}N_1Se_{24}$ supercell, **(c)** $Sb_{16}Se_{23}N_1$ supercell.

performed additional computations with different DFT methods: local density approximation [44] and different functionals (PBE [38], RPBE [45], PW91 [46], and PBESOL [47]) in the generalized gradient approximation (GGA). The details of these computations are provided in the supporting information file.

3 Results and discussion

3.1 Structural optimization

Pure antimony triselenide structure was optimized before calculating the electronic structures, which were then used to find the lattice parameters minimizing the energy. Shown in Table 1, the computationally calculated results for the structural parameters a, b, c, and V are compared with the known experimental values [36] and previous theoretical results [39, 48]. The lattice parameters calculated in this work are in accordance with the experimental data.

Table 1 Optimized structural parameters for $Sb_{16}Se_{24}$ compared with experimental and previous theoretical results.

	Exp. [36]	Present work		LDA [48]		GGA [39]	
		Result	Dev (%)	Result	Dev (%)	Result	Dev (%)
a (Å)	11.62	11.451	−1.45	11.22	−3.44	11.7	+0.69
b (Å)	11.77	11.862	+0.78	11.52	−2.12	11.91	+1.19
c (Å)	3.962	3.947	−0.38	3.96	−0.05	3.98	+0.45
V (Å^3)	541.87	536.24	−1.04	511.84	−5.54	554.60	+2.35

3.2 Formation energy and cohesive energy

A smaller value of formation energy shows that a reaction from pure elements to final compounds is possible. Similarly, a smaller value of cohesive energy indicates that the final compounds are energetically stable. The energies are defined as follows for N-doping at Sb and Se sites:

$$E_f(x) = \left[E^{doped}_{total}(x) - (16-x)E^{Sb}_{crystal} - 24E^{Se}_{crystal} - x\frac{1}{2}E^{N2}_{gas}\right]/40, \tag{1}$$

$$E_f(x) = \left[E^{doped}_{total}(x) - 16E^{Sb}_{crystal} - (24-x)E^{Se}_{crystal} - x\frac{1}{2}E^{N2}_{gas}\right]/40, \tag{2}$$

$$E_c(x) = \left[E^{doped}_{total}(x) - (16-x)E^{Sb}_{atom} - 24E^{Se}_{atom} - x\frac{1}{2}E^{N}_{atom}\right]/40, \tag{3}$$

$$E_c(x) = \left[E^{doped}_{total}(x) - 16E^{Sb}_{atom} - (24-x)E^{Se}_{atom} - x\frac{1}{2}E^{N}_{atom}\right]/40. \tag{4}$$

Here, $E^{doped}_{total}(x)$, $E^{Sb}_{crystal}$, $E^{Se}_{crystal}$, E^{N2}_{gas}, E^{Sb}_{atom}, E^{Se}_{atom}, and E^{N}_{atom} are the total energies of $Sb_{(16-x)}Se_{24}N_x$, $Sb_{16}Se_{(24-x)}N_x$, Sb, and Se crystals in their most stable phases and N_2, Sb, Se, and N atoms, respectively. $x(N1, N2)$, x is the number of doped atoms out of the 40 atoms in the supercell.

Figure 2 shows the formation energy and cohesive energy for $Sb_{16}Se_{24}$, $Sb_{15}N_1Se_{24}$, $Sb_{14}N_2Se_{24}$, $Sb_{16}Se_{23}N_1$, and $Sb_{16}Se_{22}N_2$. Both the formation energy and cohesive energy increase for N-doping at Sb and Se sites as the concentration of N increases, which indicates that N-doping at Se sites is more energetically favorable than at Sb sites. The energy required for the reaction increases in the following order: $Sb_{16}Se_{23}N_1 > Sb_{16}Se_{22}N_2 > Sb_{15}N_1Se_{24} > Sb_{14}N_2Se_{24}$, so the stability of the final compounds increases in the reverse order. Therefore, we can conclude that $Sb_{16}Se_{23}N_1$ is the most favorable configuration.

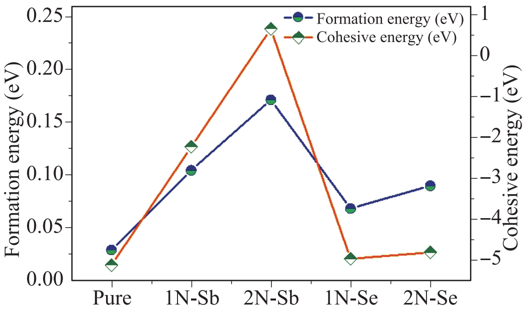

Fig. 2 The formation energy and cohesive energy for $Sb_{16}Se_{24}$, $Sb_{15}N_1Se_{24}$, $Sb_{14}N_2Se_{24}$, $Sb_{16}Se_{23}N_1$, and $Sb_{16}Se_{22}N_2$.

3.3 Band structure

The electronic band structures of pure and nitrogen-doped antimony selenides were calculated in the first Brillouin zone (BZ) along high symmetry directions. High-symmetry points $G(0,0,0)$, $F(0,1/2,0)$, $Q(0,1/2,1/2)$, and $Z(0,0,1/2)$ were used to calculate the band structures. The band structures of $Sb_{16}Se_{24}$, $Sb_{15}N_1Se_{24}$, and $Sb_{16}Se_{23}N_1$ are displayed in Fig. 3(a)–(c) and those of $Sb_{15}N_2Se_{24}$and $Sb_{16}Se_{23}N_2$ are given in the supporting information file (Figs. S2 and S3).

It is clear from the energy band structure in Fig. 3(a), in particular, from the difference between the valence band maximum (VBM) and conduction band minimum (CBM), that Sb_2Se_3 is an indirect bandgap semiconductor material. Our calculations are consistent with previous DFT calculations [3, 42, 58]. There is a difference between the calculated and experimental values of the bandgap of pure Sb_2Se_3. The calculated value of the bandgap is 0.870 eV, while the experimental value is 1.11–1.17 eV [49–51]. The calculated value is underestimated. Such underestimation is caused by neglecting the discontinuity in the exchange correlation potential and by the poor description of strong Coulomb correlation [52] and can be corrected by using a scissors operation. However, these results are still valuable for making qualitative statements regarding the accuracy of comparing the relevant properties of Sb_2Se_3 crystals.

In order to investigate the effect of N-doping in Sb_2Se_3, pseudopotential calculations were performed for Sb_2Se_3 with N substitution. In $Sb_{15}N_1Se_{24}$, the conduction band edge [Fig. 3(b)] shows a slight change in position towards the lower energy. The bandgap of single-atom nitrogen-doped Sb_2Se_3 is reduced from 0.870 to 0.547 eV. Additionally, two new occupied bands emerge close to −10.68 and −17.3 eV in the valence band. As a result, N-doping of the Sb_2Se_3 lattice is found to be effective since the N-2p states contribute to the bandgap narrowing by mixing with the Se-4p states. In $Sb_{15}N_2Se_{24}$, the bandgap is reduced even more than in $Sb_{15}N_1Se_{24}$. Two-atom N-doping reduces the bandgap from 0.870 to 0.447 eV. Some new occupied bands emerge here as well (see Figs. S2 and S3 in the supporting information file). This can be regarded as a defect state induced by single nitrogen atom doping.

After N-doping at Se sites, we can clearly see in Fig. 3(c) (see band structure in Fig. S2 in the supporting information file for 2N-doping at Se sites) the impurity energy level caused by introducing N. We find that for N-doping at one or two Se sites the impurity energy level of the N-2p states, which slightly intersects the Femi level, is introduced in the forbidden band. In particular, the N-2p states and Se-2p states display a slight overlap indicating the bonding interactions between the N and Se atoms. At the same time, the shapes of the valence and conduction bands of $Sb_2Se_{23}N_1$ and $Sb_2Se_{22}N_2$ remain unaltered.

3.4 Density of states

To get a more in-depth understanding regarding the electronic structure of pure and N-doped Sb_2Se_3, the doping dependences of the total density of states (TDOS) as well

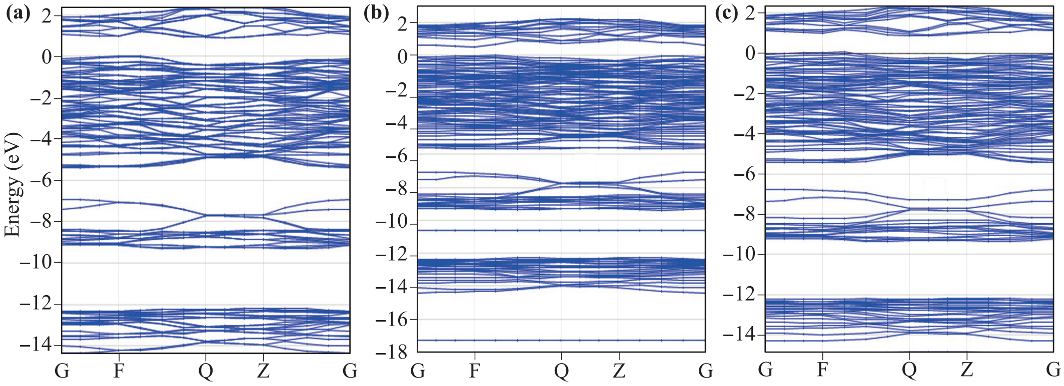

Fig. 3 Energy band structure of pure and N-doped Sb_2Se_3. The Fermi level (E_f) is at zero. **(a)** The band structure of pure Sb_2Se_3, **(b)** the band structure of $Sb_{15}N_1Se_{24}$, and **(c)** the band structure of $Sb_{16}Se_{23}N_1$.

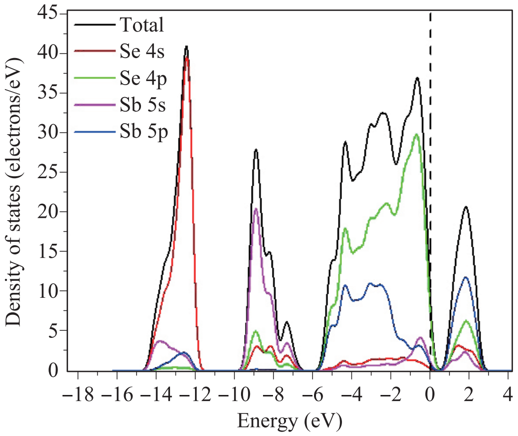

Fig. 4 The total and partial density of states of pure Sb_2Se_3.

as partial density of states (PDOS) of the N-2p states are investigated, as shown in Fig. 4 and Figs. 5(a)–(d).

Figure 4 depicts the electronic partial and total density of states of pure Sb_2Se_3 per atom (Sb and Se) and per orbital type (s and p). The lowest occurrence of the valence band between −14.7 eV and −11.6 eV is due to the domination of the Se-4s states. The intermediate occurrence of the valence band between −9.86 eV and −6.42 eV is due to the domination of the Sb-5s states. The results are consistent with those reported previously [4]. The highest occupied valence bands are effectively dominated by the Se-4p states. The lowest unoccupied conduction bands are due to the domination of the Sb-5p states. The Se-4p states also contribute to the conduction band, but the associated values of density of states are very small as compared to the Sb-5p states.

The total and partial DOS contributed by N substituted at Sb sites are shown in Fig. 5(a), where N contributes with 2s and 2p, Sb with 5s and 5p, and Se with 4s and 4p states. Four modifications of the pure Sb_2Se_3 DOS are caused by introducing single-atom N-doping. First, two new peaks emerge around −17.2 eV and −10.6 eV, which are dominated by the N-2s states and the Se-4s states. Second, the height of the peaks is slightly reduced. Third, the highest occupied valence band near the Fermi energy appears due to the domination of the Se-4p states and a small contribution from the N-2p states. Finally, the highest unoccupied conduction band shifts closer to the Fermi level, which is mainly dominated by the Sb-5p states with a very small contribution of the N-2p states, in contrast to the Se-4p states. In the DOS of $Sb_{14}N_2Se_{24}$, as compared to that of $Sb_{15}N_1Se_{24}$, the new peaks exhibit slightly shifted positions, which are marginally higher than those for single-atom N-doping, and some new peaks appear in the valence band due to the N-2p states [Fig. 5(b)]. However, in the conduction band the role of the N-2p and N-2s states marginally increases with the increasing doping level. This indicates that the increase in the nitrogen concentration results in a slightly stronger electronic mixing between the N-2p and Sb-5p states.

Figures 5(c) and (d) show the TDOS and PDOS for N-doping at one and two Se sites. Introducing one N at Se sites produces almost the same modifications in the valence and conduction band as introducing one N atom at Sb sites in a pure crystal. A new peak emerges around −14.8 eV, which is dominated by the N-2s states. The highest occupied valence band near the Fermi energy is due to the domination of the Se-4p states with a small contribution from the N-2p states. The highest unoccupied conduction band shifts closer to the Fermi level, which is dominated mainly by the Sb-5p states with a very small contribution of the N-2p states, as compared to the Se-4p states in a pure crystal. Comparing $Sb_{16}Se_{22}N_2$ to $Sb_{16}Se_{23}N_1$, the new peaks are slightly higher in $Sb_{16}Se_{22}N_2$, and additional peaks appear in the valence band due to the N-2p states [Fig. 5(b)]. However, in the conduction band the role of the N-2p and N-2s states marginally increases with the increasing doping level. This indicates that the increase in the nitrogen concentration results in a slightly stronger electronic mixing between the N-2p and Sb-5p states.

3.5 Optical properties

Interaction of light with semiconductors is very important for optoelectronic and photonic devices. The frequency-dependent complex dielectric function, $\varepsilon = \varepsilon_r(\omega) + \mathrm{i}\varepsilon_i(\omega)$, is used here to calculate the optical properties. Imaginary part of dielectric function ($\varepsilon_2(\omega)$) can be thought of as a function describing real transitions between occupied and unoccupied electronic states. Since the dielectric function describes a causal response, the real and imaginary parts are linked by the Kramers-Kronig transformation. The Kramers-Kronig transformation is used in the calculation of the real part of the function from the imaginary part. The following equations are used in the calculation of the other optical constants such as the refractive index n, absorption coefficient α, and optical conductivity σ [53].

$$\varepsilon_2(\omega) = \frac{2e^2\pi}{\Omega\varepsilon_0} \sum_{k,v,c} |\Psi_k^c|u.r|\Psi_k^v| \delta(E_k^c - E_k^v - E), \tag{5}$$

$$\varepsilon_1(\omega) = 1 + \frac{2}{\pi} P \int_0^\infty \frac{\omega' \varepsilon_2(\omega')}{\omega'^2 - \omega^2} \mathrm{d}\omega', \tag{6}$$

$$n(\omega) = \frac{\sqrt{2}}{2} [\sqrt{\varepsilon_1^2(\omega) + \varepsilon_2^2(\omega)} + \varepsilon_1(\omega)]^{\frac{1}{2}}, \tag{7}$$

$$\alpha(\omega) = \sqrt{2} [\sqrt{\varepsilon_1^2(\omega) + \varepsilon_2^2(\omega)} - \varepsilon_1(\omega)]^{\frac{1}{2}}, \tag{8}$$

$$\sigma(\omega) = \mathrm{Re}\left(-\mathrm{i}\frac{\omega}{4\pi}(\varepsilon(\omega) - 1)\right). \tag{9}$$

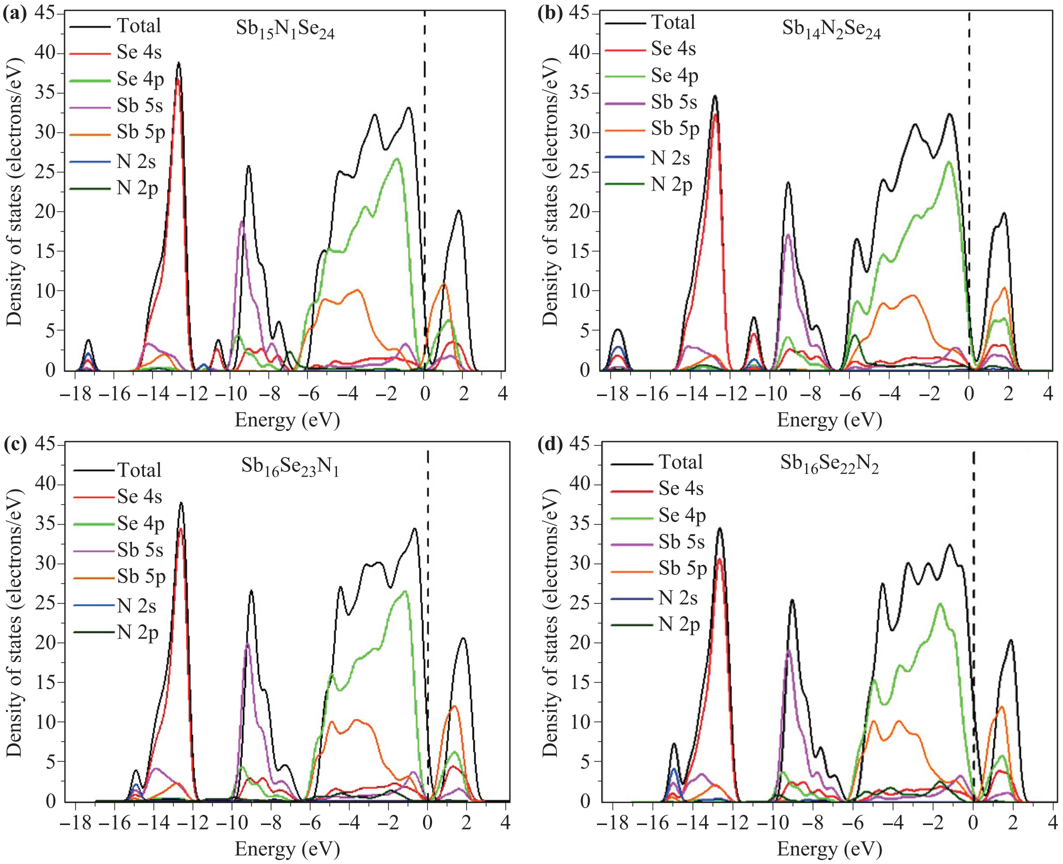

Fig. 5 The total and partial density of states of **(a)** $Sb_{15}N_1Se_{24}$, **(b)** $Sb_{14}N_2Se_{24}$, **(c)** $Sb_{16}Se_{23}N_1$, and **(d)** $Sb_{16}Se_{22}N_2$, respectively.

In the equations, u is the polarization of the incident electric field, ω is the frequency of light, e is the electron charge, and ψ_k^c and ψ_k^v are the conduction and valence band wave functions at k, respectively. Principle value is indicated by P in front of the integral sign. "Scissors approximation" [54] is used to match the theoretical bandgap to the experimental bandgap in the present work. The value of the scissor cut is set as 0.240 eV for doped and undoped $1 \times 1 \times 2$ supercells of Sb_2Se_3.

3.5.1 Complex dielectric function

Figure 6 and Fig. 7 illustrate the real and imaginary components of the dielectric function of $Sb_{16}Se_{24}$, $Sb_{15}N_1Se_{24}$, $Sb_{14}N_2Se_{24}$, $Sb_{16}Se_{23}N_1$, and $Sb_{16}Se_{22}N_2$ obtained from Equation 6. For an undoped Sb_2Se_3 crystal, $\mathcal{E}_1(\omega)$ reaches a peak around 1.5 eV, crosses zero at 2.80 and again crossing zero at 10.26 eV, and eventually becomes negative and reaches a minimum. Similarly, for $Sb_{15}N_1Se_{24}$, almost the same steep monotonous decrease in $\mathcal{E}_1(\omega)$ and a peak at the same location are observed. But in the case of 2N doping, $\mathcal{E}_1(\omega)$ shows a slightly different behavior, exhibiting a peak at 1.10 eV, crossing zero at 2.34 and 8.41 eV, turning negative, and finally reaching a minimum. Except for a higher static dielectric constant $\mathcal{E}_1(0)$ of $Sb_{16}Se_{23}N_1$ as compared to $Sb_{15}N_1Se_{24}$, it can be seen from Fig. 6(b) that all other modifications are the same. But in $Sb_{16}Se_{22}N_2$, the static dielectric constant $\mathcal{E}_1(0)$ exhibits a much higher value (39.29 eV), and the dielectric function shows a sudden drop away from zero frequencies, as compared to other doping configurations.

A characteristic frequency at which the response of a material changes from metallic to dielectric is called the plasma frequency ω_p. It is defined as the higher frequency at which the real part of the dielectric function vanishes $\varepsilon_1(\omega p) = 0$. The static dielectric constant $\mathcal{E}_1(0)$ is defined by the low-frequency limit of $\mathcal{E}_1(\omega)$. The obtained optical dielectric constants of undoped and doped Sb_2Se_3 systems are listed in Table 2.

The imaginary part of the dielectric function $\mathcal{E}_2(\omega)$ (Fig. 7) can be calculated from Eq. (5). In a pure crystal, the transitions occur from the Se-4p to Sb-5p states, while for N-doping at Sb and Se sites the transitions occur from the Se-4p and N-2p to Sb-5p states. In this study, we consider the dielectric function $\mathcal{E}_2(\omega)$ in the energy range of 0.1–8 eV. For a pure crystal, a peak ap-

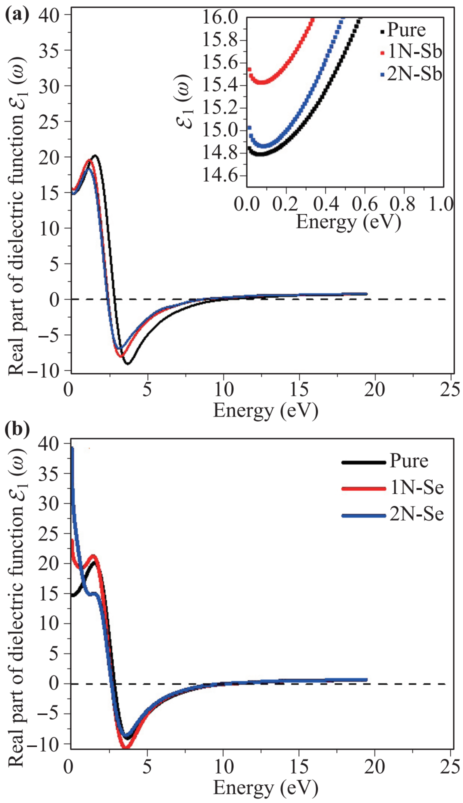

Fig. 6 The real part of the dielectric function ($\mathcal{E}_1(\omega)$) of **(a)** $Sb_{16}Se_{24}$, $Sb_{15}N_1Se_{24}$, and $Sb_{14}N_2Se_{24}$, with the inset showing a zoomed-in low-frequency range, and **(b)** $Sb_{16}Se_{24}$, $Sb_{16}Se_{23}N_1$, and $Sb_{16}Se_{22}N_2$.

pears at about 2.56 eV, which is assigned to the transition from the highest valence band towards the lowest valence band. For $Sb_{15}N_1Se_{24}$, the peak occurs at about 2.13 eV. As seen in Fig. 7(a), the peaks are shifted from higher to lower energies, as compared to an undoped system. Similar modifications are observed in $Sb_{14}N_2Se_{24}$. The peak slightly shifts towards low energies and decreases to 2.08 eV, as compared to $Sb_{15}N_1Se_{24}$. The shift of the peaks in both systems can be associated with the transitions between the Sb-5p and the unoccupied N-2p states and variations of the band structure. In $Sb_{16}Se_{23}N_1$ and $Sb_{16}Se_{22}N_2$, the peaks are slightly shifted towards low energies, and occur at about 2.4 eV [see Fig. 7(b)]. The peak shows a minor increase in $Sb_{16}Se_{23}N_1$ and a considerable decrease in the case of 2N doping. However, there is a noticeable change in the zero-frequency values: as the N concentration increases, the zero-frequency value of the imaginary part of the dielectric function increases too. This represents the increased energy loss in

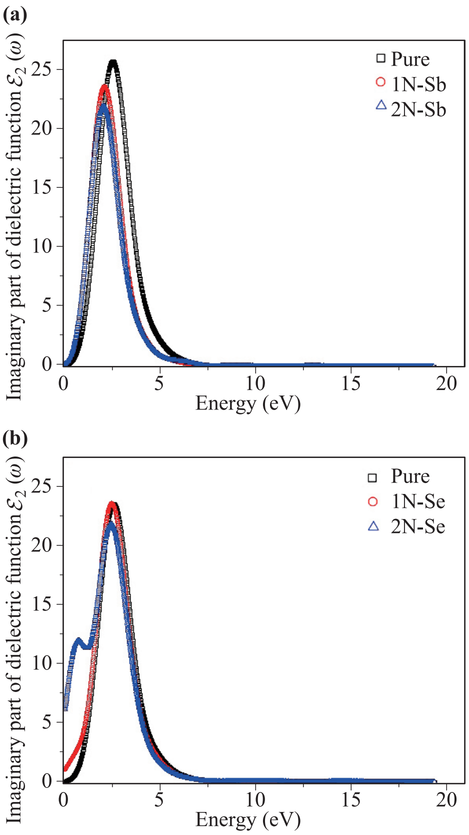

Fig. 7 The imaginary part of the dielectric function ($\mathcal{E}_2(\omega)$) of **(a)** $Sb_{16}Se_{24}$, $Sb_{15}N_1Se_{24}$, and $Sb_{14}N_2Se_{24}$, with the inset showing the zoomed-in low-frequency region, and **(b)** $Sb_{16}Se_{24}$, $Sb_{16}Se_{23}N_1$, and $Sb_{16}Se_{22}N_2$.

Table 2 Summary of the optical properties of $Sb_{16}Se_{24}$, $Sb_{15}N_1Se_{24}$, $Sb_{14}N_2Se_{24}$, $Sb_{16}Se_{23}N_1$, and $Sb_{16}Se_{22}N_2$.

Property	Previous work	$Sb_{16}Se_{24}$	$Sb_{15}N_1Se_{24}$	$Sb_{14}N_2Se_{24}$	$Sb_{16}Se_{23}N_1$	$Sb_{16}Se_{22}N_2$
Static dielectric $\mathcal{E}_1(0)$	10.7–18 [49, 50, 60]	14.84	15.54	15.02	18.9	39.29
Screen plasma frequency	7.58 eV [64]	10.01 eV	8.62 eV	8.43 eV	9.81 eV	9.72 eV
Dielectric imaginary part $\mathcal{E}_2(\omega)$ peaks	2.78 eV [4]	2.56 eV	2.13 eV	2.08 eV	2.46 eV	2.43 eV
Refractive index $n(0)$	3.69–3.82 [50, 60]	3.83	3.92	3.86	4.33	6.21
Absorption intense peak	2.78 eV [4]	3.77 eV	3.33 eV	3.30 eV	3.68 eV	3.78 eV
Conductivity intense peak	2.70 eV [60]	2.80 eV	2.40 eV	2.34 eV	2.70 eV	2.67 eV

the doped medium due to the orientation of the dipoles opposite to random collisions in electric filed.

3.5.2 Complex refractive index

Equation (7) shows the relationship between the complex dielectric function and refractive index. The refractive index of $Sb_{16}Se_{24}$, $Sb_{15}N_1Se_{24}$, $Sb_{14}N_2Se_{24}$, $Sb_{16}Se_{23}N_1$, and $Sb_{16}Se_{22}N_2$ is shown in Fig. 8. Table 2 shows the static refractive index for undoped and N-doped Sb_2Se_3. At low frequency $\omega(0)$, $n(0) = \sqrt{\mathcal{E}_1(0)}$ relation is used for $n(0)$ and $\mathcal{E}_1(0)$. The calculated static refractive index $n(0)$ is 3.84. This value is close to 3.90 that is reported by El-Sayad [3].

With the increasing N concentration, the refractive index of N-doped Sb_2Se_3 exhibits different trends in $Sb_{15}N_1Se_{24}$ and $Sb_{14}N_2Se_{24}$. The refractive index is slightly higher for low N-doping as compared to pure Sb_2Se_3, whereas it shows the opposite result for high N-doping [Fig. 8(a)]. The refractive index (static) can be tuned with nitrogen doping. The main peaks in the refractive index curves are located in the range of 1.27–1.70 eV. The refractive index drops sharply when the photon energy is larger than 1.70 eV, but for the energies above 7.65 eV the refractive index is considerably higher than that of $Sb_{16}Se_{24}$. In contrast, the refractive index for N-doping at Se sites increases with the increasing N concentration, together with the static refractive index $n(0)$ [Fig. 8(b)], and no significant variations in comparison to a pure crystal are observed.

Indeed, the contribution of N-doping to the Sb_2Se_3 crystal refractive index depends on many other factors besides the dopant concentration. These include the strain caused by the dopant-induced lattice mismatch, the enhancement of the electronic polarizability of the crystal structure due to the large difference in electronic polarizability between the constituent cations and the dopant, as well as the elasto-optic effect caused by the lattice contraction or expansion. One or all of these factors may contribute to the index of refraction, and some factors may have a positive contribution while the others may have a negative contribution. The main peak of the refractive index curve varies both in magnitude and position, moving to the lower photon energies (red shift). The principal phenomenon which explains this resonance shift is the variation of the separation between the ground and the first excited states that are involved in the optical transition. Consequently, we can conclude that the concentration of the dopant can be used to control the desired refractive index changes. The high refractive index materials have attracted much attention due to their potential applications in lenses, optical filters, reflectors, antireflection films, optical waveguides, encapsulation materials for light emitting diodes (LEDs), and solar cells [55–59].

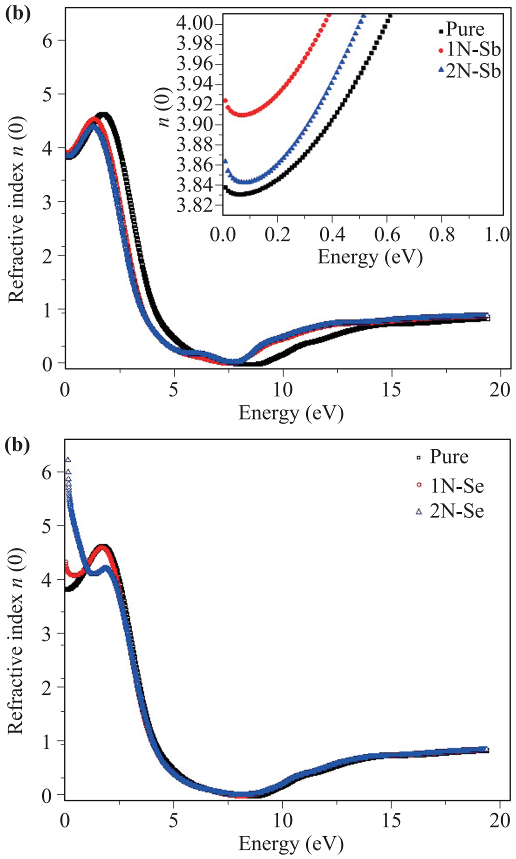

Fig. 8 The complex refractive index $n(\omega)$ of **(a)** $Sb_{16}Se_{24}$, $Sb_{15}N_1Se_{24}$, and $Sb_{14}N_2Se_{24}$, with the inset showing the zoomed-in low-frequency region, and **(b)** $Sb_{16}Se_{24}$, $Sb_{16}Se_{23}N_1$, and $Sb_{16}Se_{22}N_2$.

3.5.3 Absorption spectra

Equation (8) can be used to calculate the absorption spectra of $Sb_{16}Se_{24}$, $Sb_{15}N_1Se_{24}$, $Sb_{14}N_2Se_{24}$, $Sb_{16}Se_{23}N_1$, and $Sb_{16}Se_{22}N_2$. Figure 9 shows the spectra of Sb_2Se_3 for different doping levels. The position of the main peak ranges from 3.30 to 3.78 eV. This energy range is similar to that of the imaginary component of the dielectric function. The results for the fundamental absorption edge of $Sb_{16}Se_{24}$ are in agreement with the direct transition and band structure results (see Fig. 7). It is well-known that the absorption edge generally arises from the interband transition between the maximum of the valence band and the minimum of the conduction band. The absorption edge of undoped Sb_2Se_3 corresponds to the transitions from the Se-4*p* states to Sb-5*p* states, whereas for N-doping at Sb and Se sites it corresponds to the transitions from the Se-4*p* and N-2*p* states to Sb-5*p* states. It can be observed that the optical absorbance curves of $Sb_{15}N_1Se_{24}$ and $Sb_{14}N_2Se_{24}$ show some red shift towards the short-wave infrared spectral region. However, it is clear from

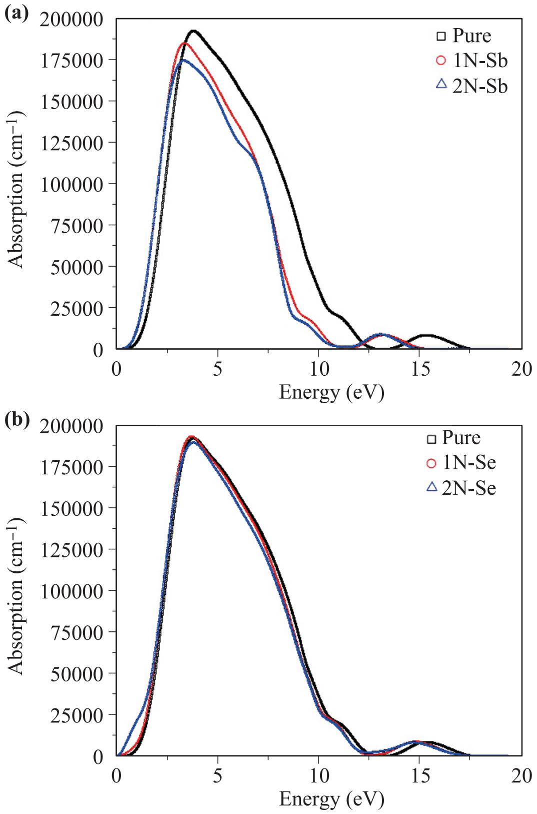

Fig. 9 The absorption spectra of **(a)** $Sb_{16}Se_{24}$, $Sb_{15}N_1Se_{24}$, and $Sb_{14}N_2Se_{24}$, and **(b)** $Sb_{16}Se_{24}$, $Sb_{16}Se_{23}N_1$, and $Sb_{16}Se_{22}N_2$.

Fig. 9(b) that there is significant variation in the absorption spectra of $Sb_{16}Se_{23}N_1$ and $Sb_{16}Se_{22}N_2$, as compared to pure Sb_2Se_3. Effective nitrogen doping integration is established by tracking the free carrier absorption in the infrared region.

3.5.4 Optical conductivity

Sb_2Se_3 is a good conductor due to the narrow bandgap; its optical conductivity is calculated by H. Maghraoui-Meherzi *et al.* [60], and has a pronounced peak at 2.70 eV, which is identical to our calculated result (Table 2). Doping with nitrogen is motivated by the improvement of the optical conductivity of Sb_2Se_3, as compared with doping by others materials, such as S, Ge, and Sn [3, 61, 62]. Figure 10 depicts the optical conductivity of undoped and doped Sb_2Se_3, which is calculated from Eq. (9). When N is introduced to antimony selenide, the conduction bands near the Fermi energy level generate a small number of N-2*s* electrons and a large number of N-2*p* electrons, which shifts the conductivity of the system at lower energies. The optical conductivity peaks of $Sb_{16}Se_{24}$, $Sb_{15}N_1Se_{24}$, $Sb_{14}N_2Se_{24}$, $Sb_{16}Se_{23}N_1$, and $Sb_{16}Se_{22}N_2$ are located at 2.80, 2.40, 2.34, 2.70, and 2.65 eV, respectively. A less pronounced shoulder between 7.80 and 15 eV can also be observed in the conductivity spectra of the doped systems. It is clear from Fig. 10 that the conductivity peaks shift toward lower energies with doping, which supports our results for $\mathcal{E}_2(\omega)$. However, the shifting of peaks for the case of N-doping at Se sites is not as much as for the case of N-doping at Sb sites.

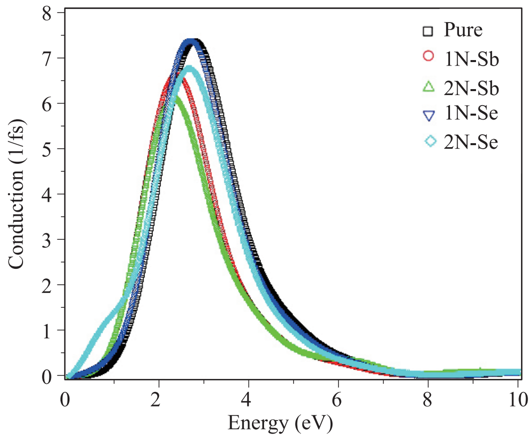

Fig. 10 The optical conductivity of $Sb_{16}Se_{24}$, $Sb_{15}N_1Se_{24}$, $Sb_{14}N_2Se_{24}$, $Sb_{16}Se_{24}$, $Sb_{16}Se_{23}N_1$, and $Sb_{16}Se_{22}N_2$.

All the optical properties including the real part of dielectric function $\mathcal{E}_1(\omega)$, imaginary part of the dielectric function $\mathcal{E}_2(\omega)$, refractive index, optical absorption, and optical conductivity are summarized in Table 2. Through the analysis and comparison, it is concluded that the effects of N-doping at Sb and Se sites are the key reasons for the Sb_2Se_3 energy bandgap narrowing and the enhancement of the optical properties in the short-wave infrared spectral region. Also, as shown in literature, N-doping is the best way to improve the optical activity and thermoelectric properties [30, 31, 63].

4 Conclusion

In summary, we present first-principles studies on the electronic structure and optical properties of N-doped Sb_2Se_3. The substitution of Sb by N atoms in the Sb_2Se_3 lattice introduces an impurity state N-2*p* in the upper valence band that results in a significant reduction of the bandgap, whereas the replacement of Se by N atoms transforms the semiconducting behavior of Sb_2Se_3 into a metallic one. Consequently, the optical properties are modified such that the dielectric function and refractive index are slightly greater in $Sb_{15}N_1Se_{24}$, but smaller in $Sb_{14}N_2Se_{24}$ than in pure Sb_2Se_3. For $Sb_{16}Se_{23}N_1$ and $Sb_{16}Se_{22}N_2$, both properties show increasing trends. This behavior is mainly determined by the intra-band level repulsion between the host states and N-induced states in the valence bands. The optical absorption and optical conductivity curves for the case of N-doping at Sb sites show a significant redshift towards the short-wave infrared spectral region as compared to the case of N-doping at Se sites. The optical properties and bandgap narrowing effect suggest that the N-doped Sb_2Se_3 is a promising new semiconductor that can be a replacement for GaSb because of the very close bandgap and low cost. In addition, nitrogen doping may be the most promising way to enhance the short-wave infrared optical activity. N-doped Sb_2Se_3 can be used for infrared detectors, infrared LEDs, lasers, and transistors, as well as thermophotovoltaic systems. This study can be generalized for non-metal doping in chalcogenides system for their exploitation in optoelectronic devices.

Electronic supplementary material Supplementary material is available in the online version of this article at https://doi.org/10.1007/s11467-018-0790-2 and is accessible for authorized users.

Acknowledgements This work was supported in part by the National Natural Science Foundation of China (Grant No. 61675195) and Sponsored by CAS-TWAS President's Fellowship for international PhD. Students, PSF project No. PSF/NSFC/Eng-P-UoL (02). F. K. Butt acknowledges the funding from Alexander von Humboldt Foundation and Federal Ministry for Education and Research (BMBF), Germany. The author (Bakhtiar Ul Haq) would like to express his gratitude to Research Center of Advanced Materials - King Khalid University, Saudi Arabia for support.

References and notes

1. L. Etgar, Semiconductor nanocrystals as light harvesters in solar cells, *Materials* 6(2), 445 (2013)
2. D. Choi, Y. Jang, J. Lee, G. H. Jeong, D. Whang, S. W. Hwang, K. S. Cho, and S. W. Kim, Diameter-controlled and surface-modified Sb_2Se_3 nanowires and their photodetector performance, *Sci. Rep.* 4, 6714, (2014)
3. E. El-Sayad, A. Moustafa, and S. Marzouk, Effect of heat treatment on the structural and optical properties of amorphous Sb_2Se_3 and Sb_2Se_2S thin films, *Physica B* 404(8–11), 1119 (2009)
4. H. Koc, A. M. Mamedov, E. Deligoz, and H. Ozisik, First principles prediction of the elastic, electronic, and optical properties of Sb_2S_3 and Sb_2Se_3 compounds, *Solid State Sci.* 14(8), 1211 (2012)
5. O. Madelung, Semiconductors: Group IV Elements and III-V Compounds, Springer Science & Business Media, 2012
6. I. H. Kim, $(Bi, Sb)_2(Te, Se)_3$-based thin film thermoelectric generators, *Mater. Lett.* 43(5), 221 (2000)
7. J. Ma, Y. Wang, Y. Wang, Q. Chen, J. Lian, and W. Zheng, Controlled synthesis of one-dimensional Sb_2Se_3 nanostructures and their electrochemical properties, *J. Phys. Chem. C* 113(31), 13588 (2009)
8. Y. Zhou, L. Wang, S. Chen, S. Qin, X. Liu, J. Chen, D. J. Xue, M. Luo, Y. Cao, Y. Cheng, E. H. Sargent, and J. Tang, Thin-film Sb_2Se_3 photovoltaics with oriented one-dimensional ribbons and benign grain boundaries, *Nat. Photonics* 9(6), 409 (2015)
9. J. Black, E. Conwell, L. Seigle, and C. Spencer, Electrical and optical properties of some M_2^{v-B} N_3^{VI-B} semiconductors, *J. Phys. Chem. Solids* 2(3), 240 (1957)
10. P. Arun, A. Vedeshwar, and N. Mehra, Laser-induced crystallization in amorphous films of (C= S, Se, Te), potential optical storage media, *J. Phys. D* 32(3), 183 (1999)
11. K. Rajpure, C. Lokhande, and C. Bhosale, Effect of the substrate temperature on the properties of spray deposited Sb–Se thin films from non-aqueous medium, *Thin Solid Films* 311(1–2), 114 (1997)
12. N. Platakis and H. Gatos, Threshold and memory switching in crystalline chalcogenide materials, *Phys. Status Solidi (a)* 13(1), K1 (1972)
13. P. M. Fourspring, D. M. DePoy, J. E. Jr Rahmlow, Lazo-Wasem, and E. J. Gratrix, Optical coatings for thermophotovoltaic spectral control, *Appl. Opt.* 45(7), 1356 (2006)
14. X. Liu, J. Chen, M. Luo, M. Leng, Z. Xia, Y. Zhou, S. Qin, D. J. Xue, L. Lv, H. Huang, D. Niu, and J. Tang, Thermal evaporation and characterization of Sb_2Se_3 thin film for substrate Sb_2Se_3/CdS solar cells, *ACS Appl. Mater. Interfaces* 6(13), 10687 (2014)
15. B. Zhou and J. J. Zhu, Microwave-assisted synthesis of Sb2Se3 submicron rods, compared with those of Bi_2Te_3 and Sb_2Te_3, *Nanotechnology* 20(8), 085604 (2009)
16. M. R. Filip, C. E. Patrick, and F. Giustino, *GW* quasiparticle band structures of stibnite, antimonselite, bismuthinite, and guanajuatite, *Phys. Rev. B* 87(20), 205125 (2013)
17. C. E. Patrick and F. Giustino, Structural and electronic properties of semiconductor-sensitized solar-cell interfaces, *Adv. Funct. Mater.* 21(24), 4663 (2011)
18. R. Vadapoo, S. Krishnan, H. Yilmaz, and C. Marin, Electronic structure of antimony selenide (Sb_2Se_3) from GW calculations, *Phys. Status Solidi B Basic Res.* 248(3), 700 (2011)
19. W. Procarione and C. Wood, The optical properties of Sb_2Se_3-Sb_2Te_3, *Phys. Status Solidi B* 42(2), 871 (1970)
20. F. Kosek, J. Tulka, and L. Štourač, Optical, photoelectric and electric properties of single-crystalline Sb_2Se_3, *Czechoslovak J. Phys. B* 28(3), 325 (1978)
21. L. Gilbert, B. Van Pelt, and C. Wood, The thermal activation energy of crystalline Sb_2Se_3, *J. Phys. Chem. Solids* 35(12), 1629 (1974)

22. S. Messina, M. Nair, and P. Nair, Solar cells with Sb_2S_3 absorber films, *Thin Solid Films* 517(7), 2503 (2009)
23. Z. S. Chu'Er Chng, M. Pumera, and A. Bonanni, Doped and undoped graphene platforms: The influence of structural properties on the detection of polyphenols, *Sci. Rep.* 6, 20673, (2016)
24. K. Chandrasekharan and A. Kunjomana, Growth and microindentation analysis of pure and doped Sb_2Se_3 crystals, *Turkish J. Phys.* 33(4), 209 (2009)
25. J. Choi, H. W. Lee, B. S. Kim, H. Park, S. Choi, S. Hong, and S. Cho, Magnetic and transport properties of Mn-doped Bi_2Se_3 and Sb_2Se_3, *J. Magn. Magn. Mater.* 304(1), e164 (2006)
26. S. Gautam, A. Thakur, S. Tripathi, and N. Goyal, Effect of silver doping on the electrical properties of a-Sb_2Se_3, *J. Non-Cryst. Solids* 353(13–15), 1315 (2007)
27. J. Li, B. Wang, F. Liu, J. Yang, J. Li, J. Liu, M. Jia, Y. Lai, and Y. Liu, Preparation and characterization of Bi-doped antimony selenide thin films by electrodeposition, *Electrochim. Acta* 56(24), 8597 (2011)
28. D. E. Reisner and T. Pradeep, Aquananotechnology: Global Prospects, CRC Press, 2014
29. T. Duan, C. Liao, T. Chen, N. Yu, Y. Liu, H. Yin, Z. J. Xiong, and M. Q. Zhu, Single crystalline nitrogen-doped InP nanowires for low-voltage field-effect transistors and photodetectors on rigid silicon and flexible mica substrates, *Nano Energy* 15, 293 (2015)
30. P. Jadaun, H. P. Nair, V. Lordi, S. R. Bank, and S. K. Banerjee, Electronic and optical properties of GaSb:N from first principles, arXiv: 1308.0363 (2013)
31. Y. Mi, S. Wang, J. Chai, J. Pan, C. Huan, Y. Feng, and C. Ong, Effect of nitrogen doping on optical properties and electronic structures of $SrTiO_3$ films, *App. Phys. Lett.* 89(23), (2006)
32. S. Qin, W. Lei, D. Liu, and Y. Chen, In-situ and tunable nitrogen-doping of MoS_2 nanosheets, *Sci. Rep.* 4, 7582, (2014)
33. H. Wang, T. Maiyalagan, and X. Wang, Review on recent progress in nitrogen-doped graphene: Synthesis, characterization, and its potential applications, *ACS Catal.* 2(5), 781 (2012)
34. X. Li, et al., Multifunctional single-phase photocatalysts: Extended near infrared photoactivity and reliable magnetic recyclability, *Sci. Rep.* 5, 15511, (2015)
35. http://www.crystallography.net/cod/9007437.html
36. N. Tideswell, F. Kruse, and J. McCullough, The crystal structure of antimony selenide, Sb_2Se_3, *Acta Crystallogr.* 10(2), 99 (1957)
37. S. J. Clark, M. D. Segall, C. J. Pickard, P. J. Hasnip, M. I. Probert, K. Refson, and M. C. Payne, First principles methods using CASTEP, *Z. Kristallogr. Cryst. Mater.* 220(5/6), 567 (2005)
38. J. P. Perdew, K. Burke, and M. Ernzerhof, Generalized gradient approximation made simple, *Phys. Rev. Lett.* 77(18), 3865 (1996)
39. N. Kuganathan, Antimony selenide crystals encapsulated within single walled carbon nanotubes-A DFT study, *J. Chem.* 6(S1), S147 (2009)
40. W. Li, X. Y. Wei, J. X. Zhu, C. Ting, and Y. Chen, Pressure-induced topological quantum phase transition in Sb_2Se_3, *Phys. Rev. B* 89(3), 035101 (2014)
41. W. Liu, X. Peng, C. Tang, L. Sun, K. Zhang, and J. Zhong, Anisotropic interactions and strain-induced topological phase transition in Sb_2Se_3 and Bi_2Se_3, *Phys. Rev. B* 84(24), 245105 (2011)
42. R. Vadapoo, S. Krishnan, H. Yilmaz, and C. Marin, Self-standing nanoribbons of antimony selenide and antimony sulfide with well-defined size and band gap, *Nanotechnology* 22(17), 175705 (2011)
43. Q. Zhang, Z. Zhang, Z. Zhu, U. Schwingenschlögl, and Y. Cui, Exotic topological insulator states and topological phase transitions in Sb_2Se_3–Bi_2Se_3 heterostructures, *ACS Nano* 6(3), 2345 (2012)
44. L. Hedin and B. I. Lundqvist, Explicit local exchange-correlation potentials, *J. Phys. C* 4(14), 2064 (1971)
45. B. Hammer, L. B. Hansen, and J. K. Nørskov, Improved adsorption energetics within density-functional theory using revised Perdew–Burke–Ernzerhof functionals, *Phys. Rev. B* 59(11), 7413 (1999)
46. J. P. Perdew, J. Chevary, S. Vosko, K. A. Jackson, M. R. Pederson, D. Singh, and C. Fiolhais, Atoms, molecules, solids, and surfaces: Applications of the generalized gradient approximation for exchange and correlation, *Phys. Rev. B* 46(11), 6671 (1992)
47. J. P. Perdew, A. Ruzsinszky, G. I. Csonka, O. A. Vydrov, G. E. Scuseria, L. A. Constantin, X. Zhou, and K. Burke, Restoring the density-gradient expansion for exchange in solids and surfaces, *Phys. Rev. Lett.* 100(13), 136406 (2008)
48. V. L. Deringer, R. P. Stoffel, M. Wuttig, and R. Dronskowski, Vibrational properties and bonding nature of Sb_2Se_3 and their implications for chalcogenide materials, *Chem. Sci.* 6(9), 5255 (2015)
49. C. Chen, D. C. Bobela, Y. Yang, S. Lu, K. Zeng, C. Ge, B. Yang, L. Gao, Y. Zhao, M. C. Beard, and J. Tang, Characterization of basic physical properties of Sb_2Se_3 and its relevance for photovoltaics, *Front. Optoelectron.* 10(1), 18 (2017)
50. C. Chen, W. Li, Y. Zhou, C. Chen, M. Luo, X. Liu, K. Zeng, B. Yang, C. Zhang, J. Han, and J. Tang, Optical properties of amorphous and polycrystalline Sb_2Se_3 thin films prepared by thermal evaporation, *Appl. Phys. Lett.* 107(4), 043905 (2015)
51. G. Y. Chen, B. Dneg, G. B. Cai, T. K. Zhang, W. F. Dong, W. X. Zhang, and A. W. Xu, The fractal splitting growth of Sb_2S_3 and Sb_2Se_3 hierarchical nanostructures, *J. Phys. Chem. C* 112(3), 672 (2008)
52. P. J. Hasnip, K. Refson, M. I. Probert, J. R. Yates, S. J. Clark, and C. J. Pickard, Density functional theory in the solid state, *Phil. Trans. R. Soc. A* 372 (2011), 20130270 (2014)

53. S. Xuechu, Semiconductor Spectra and Optical Properties, 2nd Ed., Beijing: Science Press, 1992
54. Z. H. Levine and D. C. Allan, Linear optical response in silicon and germanium including self-energy effects, *Phys. Rev. Lett.* 63(16), 1719 (1989)
55. K. C. Krogman, T. Druffel, and M. K. Sunkara, Anti-reflective optical coatings incorporating nanoparticles, *Nanotechnology* 16(7), S338 (2005)
56. J. Liu and M. Ueda, High refractive index polymers: Fundamental research and practical applications, *J. Mater. Chem.* 19(47), 8907 (2009)
57. M. Ma, F. W. Mont, D. J. Poxson, J. Cho, E. F. Schubert, R. E. Welser, and A. K. Sood, Enhancement of photovoltaic cell response due to high-refractive-index encapsulants, *J. Appl. Phys.* 108(4), 043102 (2010)
58. F. W. Mont, J. K. Kim, M. F. Schubert, E. F. Schubert, and R. W. Siegel, High-refractive-index TiO_2-nanoparticle-loaded encapsulants for light-emitting diodes, *J. Appl. Phys.* 103(8), 083120 (2008)
59. B. Ung, A. Dupuis, K. Stoeffler, C. Dubois, and M. Skorobogatiy, High-refractive-index composite materials for terahertz waveguides: Trade-off between index contrast and absorption loss, *JOSA B* 28(4), 917 (2011)
60. H. Maghraoui-Meherzi, T. B. Nasr, N. Kamoun, and M. Dachraoui, Structural, morphology and optical properties of chemically deposited Sb_2S_3 thin films, *Physica B* 405(15), 3101 (2010)
61. K. Aly, A. Abousehly, M. Osman, and A. Othman, Structure, optical and electrical properties of $Ge_{30}Sb_{10}Se_{60}$ thin films, *Physica B* 403(10–11), 1848 (2008)
62. D. Harea, M. Iovu, O. Iaseniuc, E. Colomeico, A. Meshalkin, and M. Iovu, Modification of the optical constants in amorphous Sb_2Se_3:Sn thin films under the illumination and heat treatment, *J. Optoelectron. Adv. Mater.* 11(12), 2039 (2009)
63. C. Zhang, Y. Jia, Y. Jing, Y. Yao, J. Ma, and J. Sun, DFT study on electronic structure and optical properties of N-doped, S-doped, and N/S co-doped $SrTiO_3$, *Physica B* 407(24), 4649 (2012)
64. A. SAEED, Ag_3SbS_3 and Sb_2Se_3 crystal as potential absorbers for photovoltaic application: DFT study mohammed lawal, ahmad radzi mat isah and muhammad, Proceeding of 2nd International Science Postgraduate Conference 2014 (ISPC2014)© Faculty of Science, Universiti Teknologi Malaysia